NANO LETTERS

Letter

pubs.acs.org/NanoLett

Periodic Bicontinuous Composites for High Specific Energy Absorption

Jae-Hwang Lee,[†,§,∥] Lifeng Wang,[‡,§,⊥] Mary C. Boyce,[‡,§] and Edwin L. Thomas*[,†,§,∥]

[†]Department of Materials Science and Engineering, [‡]Department of Mechanical Engineering, and [§]Institute for Solider Nanotechnologies, Massuchusetts Institute of Technology, Cambridge, Massachusetts 02139, United States

[∥]Department of Mechanical Engineering and Materials Science, Rice University, Houston, Texas 77005, United States

[⊥]Department of Civil and Environmental Engineering, Clarkson University, Potsdam, New York 13699, United States

Supporting Information

ABSTRACT: We report on the mechanical behavior of an interpenetrating carbon/epoxy periodic submicrometer-scale bicontinuous composite material fabricated following the design principles deduced from biological composites. Using microscopic uniaxial compressive tests, the specific energy absorption is quantitatively evaluated and compared with the epoxy/air and carbon/air precursors. The carbon/epoxy material demonstrates extremely high specific energy absorption up to 720 kJ/kg and shear-dominant interphase interactions from the interlocked hard (carbon) and soft (epoxy) phases. Such bicontinuous nanocomposites are a new type of structural metamaterial with designed cell topology and mechanical anisotropy. Their inherent small length scale can play a critical role in prohibiting segregated mechanical responses leading to flaw tolerance.

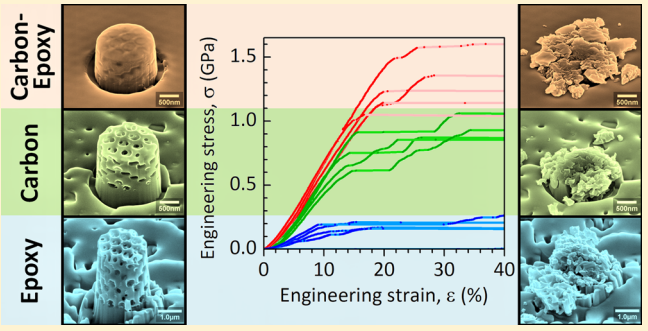

KEYWORDS: *Interpenetrating phase composite, interference lithography, protection, mechanical metamaterial, periodic frame*

Better protective materials should dissipate larger mechanical energy with equal or smaller mass than other materials.[1] In order to enhance the mechanical energy absorption per unit mass (specific energy absorption (SEA)), various macro-structured composite materials have been fabricated.[2−5] Creating a composite that can absorb more energy per unit of mass than what each of its constituent materials does in isolation is a matter of comprehensive and complex design dealing with selection of constituents (phases), interfaces between phases, and the geometrical structures of the phases. However, the design of geometrical structures at the submicrometer or in the nanoscale[6] is difficult and usually quite simplistic compared to the structures developed by nature in biological composites. Biological composites such as bones,[7] fish scales,[8] and nacres[9,10] have demonstrated exceptional protection performance via their intricate three-dimensional (3D) submicrometer-scale architectures.[11,12] Design rules deduced from the outstanding biological composites include (i) combining hard and soft materials for strength and toughness,[7,9,12] (ii) orienting structural anisotropic materials for enhanced performance in a desired direction,[7,8,13] (iii) strong 3D interlocking of phases for load sharing and energy dissipation,[12,13] and (iv) using a submicrometer scale architecture having flaw insensitivity.[14] As demonstrated at the macroscale,[15] we envisioned that an interpenetrating phase composite (IPC)[16] can potentially satisfy all the design rules simultaneously if the IPC is realized with a submicrometer scale frame architecture.[17,18]

We investigate three different classes of submicrometer-scale frameworks: epoxy-A/air nanoframe (PnF), pyrolyzed carbon/air nanoframe (CnF), and pyrolyzed carbon/epoxy-B composite nanoframes (CPnF) and focus on their energy absorption characteristics. The carbon/epoxy-B periodic bicontinuous IPC has a large interfacial surface per volume (~10 $\mu m^2/\mu m^3$) between the carbon and epoxy phases. The connectivity of the epoxy-A, carbon, and epoxy-B phases is displayed in the skeletal graph depicted in Figure 1a. In the case of the CPnF, both the carbon phase and epoxy-B phases have the same skeletal graph (self-dual structure). The aspect ratios and the orientation of the nF struts can be tailored to provide designs that enable directionally enhanced resistance as well as a multitude of deformation and fracture mechanisms that can improve energy dissipation.

These bicontinuous nanocomposites are fabricated as follows: First, a PnF (Figure 1b) is produced using an epoxy-A resin negative photoresist (see Supporting Information).[18,19] Usually, when carbonizing a PnF to convert it to a CnF (Figure 1c), strong gradients of structural deformation occur owing to

Received: June 13, 2012
Revised: July 10, 2012
Published: July 11, 2012

   dx.doi.org/10.1021/nl302234f | *Nano Lett.* 2012, 12, 4392−4396

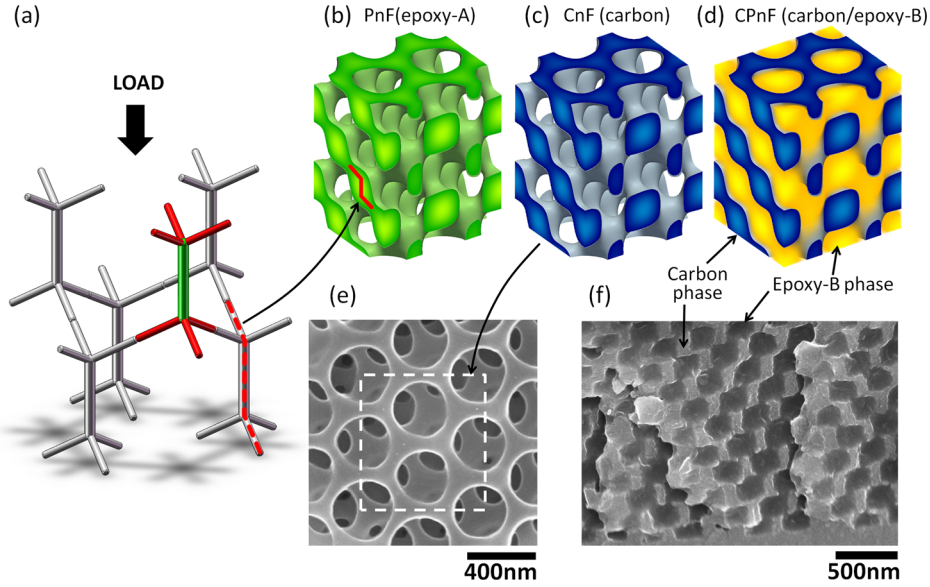

Figure 1. (a) A skeletal graph shows the connectivity of the nanoframes with the basic motif consisting of a thick vertical post (green) and six thinner side struts. A compressive load is applied along the [111]-direction of the structure. (b–d) Perspective illustration of 1 × 2 cells for each type of nanoframe. The PnF and CnF are illustrated at the same scale, (ignoring the epoxy-A shrinkage due to carbonization). (e) A top view scanning electron microscope (SEM) image of a CnF. The white dashed box outlines the same top surface area shown in (c). (f) Periodic interpenetrating carbon and epoxy-B phases are shown in a SEM image of a tensile fractured surface of a CPnF. Note the excellent filling by the epoxy-B and the absence of voids.

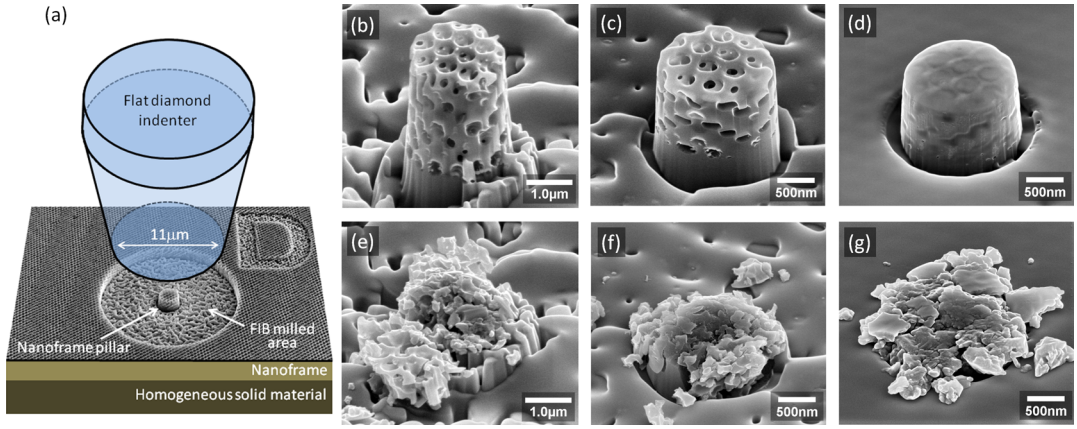

Figure 2. (a) Schematic illustration of the compression experiment. SEM images of (b) PnF, (c) CnF, and (d) CPnF pillars. (e–g) SEM images after uniaxial compression tests. All SEM images are taken at a tilt angle of 52° to the vertical axis of the pillars. Note that the diameter of the PnF pillar is larger than those of the CnF and CPnF pillars while each has the same number of unit cells.

the large mass loss ($m/\ m_0 \sim 0.4$) and densification ($\rho/\rho_0 \sim 1.7$).[20] To circumvent this problem, we fabricated the PnF on a 20 μm thick uniformly cross-linked epoxy-A film that then acts as a pliable substrate during the carbonization, allowing the PnF and the substrate epoxy-A film to shrink together. Some anisotropic shrinkage of the PnF is observed approximately 20 and 40% in the lateral and vertical directions but without noticeable overall pattern collapse or distortion (Figure 1e). After the carbonization, the Young's modulus of the epoxy-A (2.7 GPa) is significantly increased to 30 GPa along with a density increase from 1.2 to 2.0 g/cm^3. All PnF and CnF have a porosity in the range of 30–40%. CPnF can then be fabricated by infiltration of the CnF with the epoxy-B monomer (Figure 1d). The polymerized epoxy B has a density and Young's modulus of 1.05 g/cm^3 and 1.37 GPa respectively. The CPnF was tensile-fractured to confirm completeness of the epoxy-B infiltration and interlocking of the two phases (see Figure 1f). Interlocking can be effective in preventing the typical dominant failure mode of interfacial debonding in composites. Fracture faces tend to run along a low index crystal plane, and the CPnF acts as a monolithic material.

Assessment of the energy absorption capabilities of the three types of structures is carried out by microscopic uniaxial compression tests of pillar-shaped test regions presenting a well-defined compression volume and without imposing significant strain gradients (Figure 2a). Young's moduli from the compression tests of homogeneous solid pillars of epoxy-A, epoxy-B, and carbonized epoxy-A show values of 2.6, 1.4, and 32 GPa, respectively, which in good agreement with the values measured from macroscopic samples and validating the microcompression tests (see Supporting Information). In the compression tests, all micropillars are completely crushed to estimate the maximum attainable energy absorption (Figure 2e–g). The structures show brittle-like behavior with each pillar

dx.doi.org/10.1021/nl302234f | *Nano Lett.* 2012, 12, 4392–4396

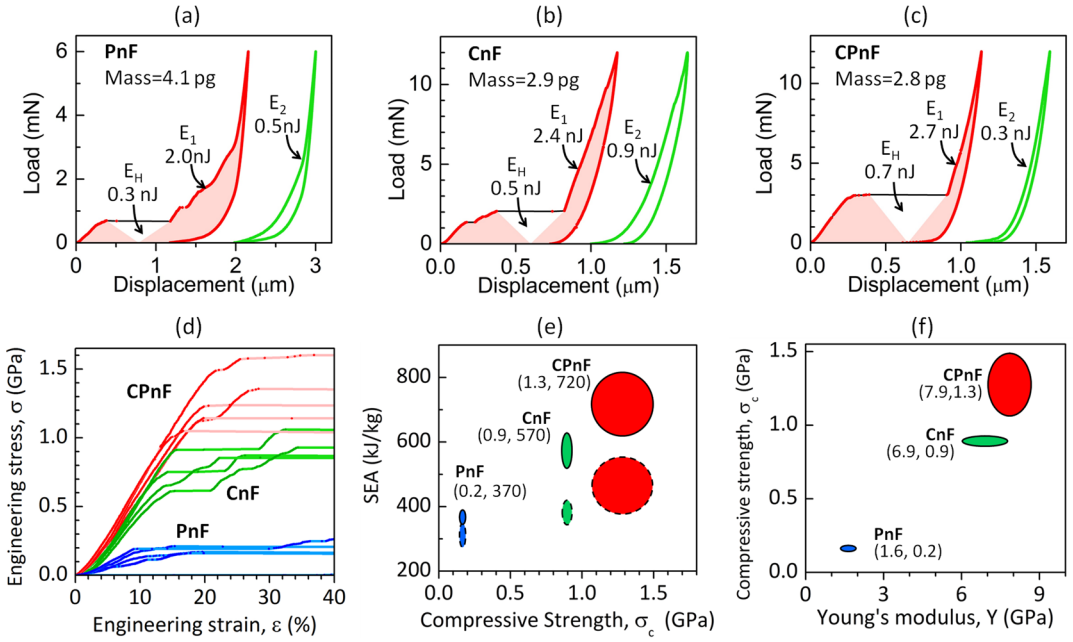

Figure 3. Load versus displacement curves for (a) PnF, (b) CnF, and (c) CPnF are shown with values of pillar mass and energy absorbed. Red and green lines show measured data points. The second loading−unloading curve in each plot is purposely shifted. (d) Engineering stress−strain from the first loading curves of all tested pillars. Actual data points are shown in darker color. (e) Ranges of the upper limit (solid line) and lower limit (dashed line) of SEA of the three materials versus compressive strength. (f) Ranges of the compressive strength versus Young's modulus. In panels e and f, all the ranges are given by the standard deviation values of the measured values. The numbers in the parentheses are the coordinates representing the average values of the data points.

comminuted into myriad of small fragments. Finite element analysis (FEA) indicates that the narrow necks in the struts of the basic motif are the most likely locations for initiation of fracture. On the basis of the multiplicity of these regions per unit cell, there are ∼100 necks per cubic micrometer of material, assuring a very high density of damage. This designed microfragmentation accompanying multiple cracking and secondary interaction among tiny brittle fragments during densification is essential for increasing the SEA, enabling higher energy absorption than monolithic ductile materials.[2] In contrast to the PnF and CnF, the fragments of the CPnF are more retained at the collapsed site in Figure 2g since the more ductile epoxy-B phase constrains the brittle carbon fragments. This feature can potentially improve endurance against multiple impacts as well as enable additional fracture events along the same strut, further enhancing SEA.

The area bounded by the loading/unloading curves should be considered as the upper limit of energy absorption (denoted as E_1) due to the lack of data points during pillar collapse. To estimate the lower limit, we add a hypothetical stress value of zero at the middle of the two strains before and after the collapse and calculate the reduced energy absorption as equal to $(E_1 - E_H)$, as shown as the shaded areas in Figure 3a−c. One additional cycle of loading and unloading on the collapsed pillars was carried out to further refine our estimate of the energy absorption by assessing the amount of energy dissipated by the substrate, the sample mounting glue and the indenter (denoted as E_2). The maximum and minimum energy absorptions values are now defined as $(E_1 - E_2)$ and $(E_1 - E_2 - E_H)$.

The stress−strain plot in Figure 3d allows direct comparison of the three different types of pillars in terms of modulus and compressive strength (σ_c). Surprisingly, all pillars can undergo significant compression to over 10% strain without failure. This seems peculiar given the brittle-like features observed from the collapsed pillars. This behavior primarily originates from the carbonized epoxy-A itself since a strain of 14% was observed at a yield point in compression tests of solid carbon pillars (see Supporting Information). Moreover, several major collapse events do not lead to the total failure of the pillar. Since in our previous study the frame geometry is known to be predominately shear-deformed,[18] the large failure strain may be due to the toughening mechanism arising from shear band deformation prior to strut collapse, which is also observed in the indentation of two-dimensional porous alumina of similar periodicity.[21]

Exceptionally high SEA values are observed in all our nanoframes: PnF (310−370 kJ/kg), CnF (380−570 kJ/kg), and CPnF (470−720 kJ/kg) (see Figure 3e). These values are considerably higher than for various advanced energy absorption materials (30−275 kJ/kg).[22−25] While the higher value of SEA of CnF over PnF can be attributed to a change of the basic material from polymer to carbon, the 25% increase in the SEA of the two-phase bicontinuous CPnF over the CnF arises from the synergic effect via introduction of the polymer phase. Note the distribution of σ_c for the CPnF is appreciably broader than for the other nFs, indicating that the CPnF pillars collapse at a broad range of stresses. As the stress exceeds the σ_c of the CnF, the CPnF pillar becomes vulnerable to catastrophic collapse but the epoxy-B phase helps to suppress the initiation of cracking and buckling of the carbon frame by redistribution of the stress. Consequently a broad range of σ_c is observed in the CPnF since failure of a few struts at low stress will not lead to overall collapse for the CPnF but will lead to collapse of the CnF. Figure 3f shows the influence of the infiltration of epoxy-B is more pronounced on the σ_c value than for the modulus; a 44% increase in σ_c with only 14% increase in modulus. This is also consistent with the role of epoxy-B in increasing σ_c by

dx.doi.org/10.1021/nl302234f | Nano Lett. 2012, 12, 4392−4396

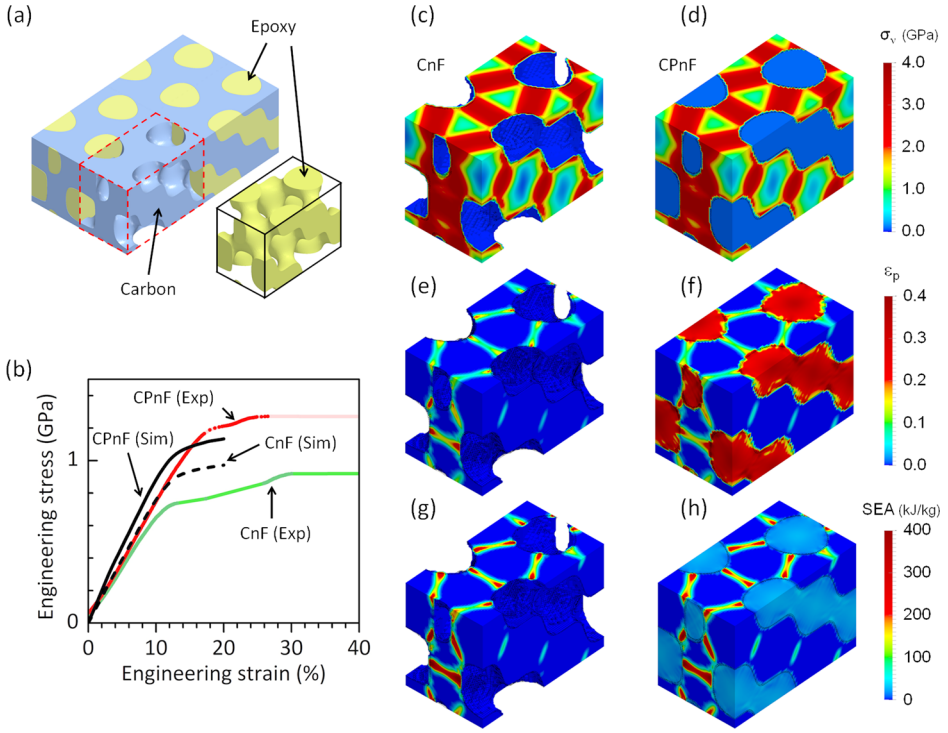

Figure 4. FEA simulation results of CPnF and CnF under uniaxial compression. (a) Representative volume element used in the FEA simulation. (b) Simulated stress–strain responses of CPnF (black solid) and CnF (black dashed) under uniaxial compression are compared with averaged stress–strain responses of all measured data. Contours of (c,d) von Mises stress, σ_v, (e,f) equivalent plastic strain, ε_p, and (g,h) local SEA of CnF and CPnF are plotted in a linear scale at a strain of 15%.

inhibiting failure and also strut buckling. Even though we have focused on the mechanical effects from the frame architecture and material bicontinuity in this study, one can expect further enhancement in SEA by choosing other polymers that can exhibit significant strain hardening with increasing deformation like the biopolymer in natural biopolymer/$CaCO_3$ composites (nacre).[26]

Next the relationship between macroscopic mechanical response and constituent material properties and geometric arrangement (Figure 4a) is numerically investigated (see Supporting Information). The simulated moduli in Figure 4b representing the elastic behavior are 7.5 GPa for CnF and 8.5 GPa for CPnF; these agree well (within 10%) with the measured values (compare Figure 4b with Figure 3f). However, the simulated yield stress of CnF (0.9 GPa) is 30% higher than the experimental value (0.7 GPa) whereas the simulated yield stress of CPnF (1.1 GPa) is still within 10% compared to the experimental value (1.2 GPa, see Figure 4b). The large discrepancy in the yield stress is most likely due to structural imperfections/defects in the actual CnF while the simulated CnF is based on an ideal, flawless structure. In the solid/air structure, such defects will govern the overall yield or collapse stress and will lead to a greatly reduced yield/collapse stress magnitude. The good agreement between the simulated and measured yield stress of the CPnF confirms that the epoxy phase in the CPnF is able to redistribute load in regions of localized early cracking initiated by the intrinsic defects present in the carbon phase and hence the bicontinuous composite is more fully able to utilize the energy dissipation of the carbon phase. Despite the relatively soft epoxy, the high shear deformation resistance of the epoxy phase arising from the large specific area imparts good flaw insensitivity of the CPnF and also suggests that an important role of the softer phase in natural hard/soft nanocomposites such as tooth and nacre is to provide load redistribution and flaw tolerance in these materials.[14]

Equivalent stress (von Mises stress, σ_v) and equivalent plastic strain (ε_p) distributions within the CPnF and CnF are compared in the postyield deformation (15% strain). Although the stress distributions in the brittle carbon phase are similar in CPnF and CnF (see Figure 4c,d) due to the relatively low modulus of the epoxy, the failure mechanisms and progression are decidedly different. In the CnF, once one strut fails, neighboring struts would overload and fail; in contrast, the CPnF is more tolerant to the initial fracturing of struts having defects and will maintain its stress distribution because of the load transfer from the epoxy. Furthermore, as compared to the highly localized small ε_p in the carbon phase, plastic strain and deformation are primarily observed in the epoxy phase where the continuous epoxy constrains the carbon phase that leads to increase in the macroscopic failure strain and promotes the advantageous noncatastrophic cracking and energy dissipation (see Figure 4e,f). The stress transfer and strain sharing mechanisms due to the presence of the epoxy phase are particularly important for interpenetrating composites with a brittle component. The local SEA contours are given by $\sigma_v(r)[\varepsilon_p(r)/\rho(r)]$ (where $\rho(r)$ is mass density) in Figure 4g,h. The CnF dissipates energy intensively only in small volumes around the struts. The carbon phase of the CPnF acts similarly but the epoxy phase adds another 50% to the dissipation by deforming throughout its whole volume but at a lower SEA intensity and also enables greater dissipation from the carbon phase due to the higher collapse stress as well as load redistribution.

In summary, significantly improved energy absorbing materials are possible by exploiting the periodic bicontinuous

dx.doi.org/10.1021/nl302234f | *Nano Lett.* 2012, 12, 4392–4396

submicrometer-scale frame architecture and offer practical opportunities to develop high-performance protective films by mechanically fusing two very different materials with high specific area into an interlocked topology. Interphase interactions such as stress transfer and strain sharing are essential to make the composite system defect-insensitive and to enhance SEA. As numerous geometrical and material variations are possible, for example, a carbon/light-metal system for protective materials of higher working temperature and conductivity and polymer/piezoelectric materials for responsive protective materials, this method may become an important means to achieve unprecedented artificial nanocomposite materials in the future.

■ ASSOCIATED CONTENT

Ⓢ Supporting Information

Detailed information of fabrication, mechanical characterization using microscopic uniaxial compression, and finite element modeling. This material is available free of charge via the Internet at http://pubs.acs.org.

■ AUTHOR INFORMATION

Corresponding Author

*E-mail: elt@rice.edu.

Notes

The authors declare no competing financial interest.

■ ACKNOWLEDGMENTS

This research was supported (in part) by the U.S. Army Research Office under contract W911NF-07-D-0004.

■ REFERENCES

(1) Thomas, E. L.; McGrath, M. F.; Buchanan, R. C.; Chelluri, B.; Haber, R. A.; Hutchinson, J. W.; Johnson, G. R.; Kumar, S. *Opportunities in protection materials science and technology for future Army applications*; National Academies Press: Washington, DC, **2011**.
(2) Hogg, P. J. *Science* **2006**, *314*, 1100.
(3) Ochelski, S.; Gotowicki, P. *Compos. Struct.* **2009**, *87*, 215.
(4) Aneziris, C. G.; Berek, H.; Hasterok, M.; Biermann, H.; Wolf, S.; Kruger, L. *Adv. Eng. Mater.* **2010**, *12*, 197.
(5) Jovicic, J.; Zavaliangos, A.; Ko, F. *Composites, Part A* **2000**, *31*, 773.
(6) Sun, L. Y.; Gibson, R. F.; Gordaninejad, F.; Suhr, J. *Compos. Sci. Technol.* **2009**, *69*, 2392.
(7) Tai, K.; Dao, M.; Suresh, S.; Palazoglu, A.; Ortiz, C. *Nat. Mater.* **2007**, *6*, 454.
(8) Bruet, B. J. F.; Song, J. H.; Boyce, M. C.; Ortiz, C. *Nat. Mater.* **2008**, *7*, 748.
(9) Li, X. D.; Chang, W. C.; Chao, Y. J.; Wang, R. Z.; Chang, M. *Nano Lett.* **2004**, *4*, 613.
(10) Huang, Z. W.; Li, H. Z.; Pan, Z. L.; Wei, Q. M.; Chao, Y. J.; Li, X. D. *Sci. Rep.* **2011**, *1*, 1.
(11) Tang, Z. Y.; Kotov, N. A.; Magonov, S.; Ozturk, B. *Nat. Mater.* **2003**, *2*, 413.
(12) Munch, E.; Launey, M. E.; Alsem, D. H.; Saiz, E.; Tomsia, A. P.; Ritchie, R. O. *Science* **2008**, *322*, 1516.
(13) Han, L.; Wang, L. F.; Song, J. H.; Boyce, M. C.; Ortiz, C. *Nano Lett.* **2011**, *11*, 3868.
(14) Gao, H. J.; Ji, B. H.; Jager, I. L.; Arzt, E.; Fratzl, P. *Proc. Natl. Acad. Sci. U.S.A.* **2003**, *100*, 5597.
(15) Wang, L. F.; Lau, J.; Thomas, E. L.; Boyce, M. C. *Adv. Mater.* **2011**, *23*, 1524.
(16) Clarke, D. R. *J. Am. Ceram. Soc.* **1992**, *75*, 739.
(17) Wang, L.; Boyce, M. C.; Wen, C.-Y.; Thomas, E. L. *Adv. Funct. Mater.* **2009**, *19*, 1343.
(18) Lee, J. H.; Wang, L. F.; Kooi, S.; Boyce, M. C.; Thomas, E. L. *Nano Lett.* **2010**, *10*, 2592.
(19) Campbell, M.; Sharp, D. N.; Harrison, M. T.; Denning, R. G.; Turberfield, A. J. *Nature* **2000**, *404*, 53.
(20) Burckel, D. B.; Washburn, C. M.; Raub, A. K.; Brueck, S. R. J.; Wheeler, D. R.; Brozik, S. M.; Polsky, R. *Small* **2009**, *5*, 2792.
(21) Xia, Z.; Riester, L.; Curtin, W. A.; Li, H.; Sheldon, B. W.; Liang, J.; Chang, B.; Xu, J. M. *Acta Mater.* **2004**, *52*, 931.
(22) Zhang, Q.; Zhao, M. Q.; Liu, Y.; Cao, A. Y.; Qian, W. Z.; Lu, Y. F.; Wei, F. *Adv. Mater.* **2009**, *21*, 2876.
(23) Liu, Y.; Qian, W. Z.; Zhang, Q.; Cao, A. Y.; Li, Z. F.; Zhou, W. P.; Ma, Y.; Wei, F. *Nano Lett.* **2008**, *8*, 1323.
(24) Schramm, J. P.; Hofmann, D. C.; Demetriou, M. D.; Johnson, W. L. *Appl. Phys. Lett.* **2010**, *97*, 241910.
(25) Yu, C. C.; Chen, Z. G.; Li, H.; Turner, J.; Zeng, X. C.; Jin, Z. H.; Jiang, J. Y.; Youssef, B.; Tan, L. *Adv. Mater.* **2010**, *22*, 4457.
(26) Xu, Z. H.; Li, X. D. *Adv. Funct. Mater.* **2011**, *21*, 3883.